Machine learning-based prediction of spatially and frequency-selective optical field coupled absorption in random metasurfaces

View Online   Export Citation   CrossMark

Meng Xu,[1,2] Zhipeng Ding,[1] Wei Su,[1,a] Bin Tang,[3] and Hongbing Yao[1,a]

AFFILIATIONS

[1]College of Mechanics and Engineering Sciences, Hohai University, Nanjing 211100, China
[2]Key Laboratory of Quantum Materials and Devices of Ministry of Education, School of Physics, Southeast University, Nanjing 211189, China
[3]School of Microelectronics and Control Engineering, Changzhou University, Changzhou 213164, China

[a]Authors to whom correspondence should be addressed: opticsu@hhu.edu.cn and alenyao@hhu.edu.cn

ABSTRACT

Achieving frequency and spatially selective optical field coupling represents a crucial avenue for simplifying metasurface architectures. Given the intricacy of promptly analyzing the optical properties of micro- and nano-devices with numerous structural parameters, this study develops a high-performance prediction terahertz (THz) metasurface model based on machine learning. A core objective of the model is to qualitatively assess the significance and impact direction of each parameter. The investigation systematically evaluates two models (uniform and linear) comprising randomly distributed micrometer resonance spheres. The optimized metasurfaces exhibit remarkable performance, achieving average absorptions of up to 86.12% and 87.82% across the 1–10 THz band range. The resonant fields are distributed in distinct spatial regions at different frequencies, showcasing selectivity in coupling spatial and frequency optical fields. The interpretable analysis derived from machine learning aligns closely with physical mechanism investigations based on electric field distributions, establishing a high degree of consistency. This convergence opens innovative perspectives for designing high-performance THz wave micro- and nano-devices.

I. INTRODUCTION

With the rapid advancement of terahertz (THz) technology, its applications have expanded to wireless communication, nondestructive testing, high-precision sensing, and other domains.[1–3] The large bandwidth and high coherence of THz waves make them increasingly pivotal in these areas.[4,5] For integrated devices seeking effective manipulation of THz waves, the development of ultrathin, broadband, and efficient THz absorbers has become a central focus in current research.

The unique physical properties of metasurfaces offer opportunities for controlling electromagnetic waves through various means, including anomalous reflection, transmission, and absorption.[6–14] Metasurfaces provide a practical avenue for achieving narrow-band, multi-band, and broadband absorption of electromagnetic waves.[15–17] Since the inception of metasurface-based electromagnetic wave

absorbers in 2008,[18] efficient wave absorption has been a focal point, particularly for broadband absorption, which holds significant promise in applications such as military stealth, radiation cooling, and solar cells.

Due to the limited interaction between THz waves and materials, achieving broadband absorption often necessitates the integration of multiple resonators within the metasurface, such as multilayer stacked pyramids and all-dielectric metasurfaces.[19–21] The advent of two-dimensional materials like graphene and black phosphorus offers potential solutions to overcome ohmic loss limitations and expand the design space for the on-chip integration of THz active electronic devices.[22–24] However, these methods require highly precise nano-patterned processing, limiting the broader application of metasurfaces. Moreover, the increasing complexity of design structures has revealed drawbacks in traditional manual

optimization methods, where designing high-performance micro–nano devices often involves thousands of optimization iterations, incurring significant time and cost. With the development of artificial intelligence technology, machine learning provides a powerful tool to develop nonintuitive advanced metasurface designs and enhance optical performance with inverse design and interpretable modeling.[25–27]

In this study, we propose a randomized metasurface based on the concept of randomly generated micrometer resonators, aiming to achieve efficient absorption of THz waves. This design is versatile and easier to process compared to conventional absorbers based on graphene or other nanostructures. We systematically discuss both distribution modes of microspheres (uniform and linear models) in conjunction with machine learning during the design process. Machine learning models of optical properties are developed for various structural parameters in different models, and optimal parameters are discussed. The effects of these parameters are systematically analyzed using interpretable machine learning analyses and validated with physical analyses such as electric fields. The absorption characteristics of electromagnetic waves in the proposed random metasurfaces exhibit significant spatial and frequency-selective responses, offering new insights into the theory of optically coupled absorption and resonance.

II. DESIGN AND THEORY

Figure 1 illustrates the comprehensive process of analyzing the absorption characteristics of coupled spatial and frequency-selective optical fields in ultrathin random metasurfaces, facilitated by a machine learning system in this study. The depicted process primarily encompasses the following steps.

We considered thin-film metasurfaces of silver (Ag) microspheres randomly distributed in a unit cell with an Ag substrate to form a functional absorption layer at the bottom. In this study, two distinct types of random metasurfaces with different spatial distributions were investigated: the uniform distribution (metal spheres randomly and uniformly distributed in the dielectric layer) and the linear distribution (where the density of metal sphere distributions gradually increases from the top to the bottom along the z axis). The dielectric layer was composed of polyethylene cyclic olefin copolymer (TOPAS), exhibiting a relative dielectric constant of 2.35, ensuring stability within the THz band.[28] The relative permittivity of Ag was determined using the classical Debye model,[29,30]

$$\varepsilon(\omega)_{Ag} = 1 - \frac{\omega_p^2}{\omega^2 - i\gamma}. \tag{1}$$

In the above equation, the values of ω_P (plasma frequency) and γ (damping constant) are set to $1.370\,36 \times 10^{16}$ and $1.717\,32 \times 10^{16}$ rad/s, respectively. In the uniform and linear models constructed, the structural parameters are divided into two main parts, which are the cell size and the distribution of Ag microspheres. The period of each cell in both x and y directions is set to P, and the height in z direction is set to h (TOPAS). The thickness of the bottom Ag layer is set to $0.5\,\mu$m, which achieves the maximum penetration depth of THz waves and can effectively reflect all the incident waves. For the Ag micrometer spheres, the
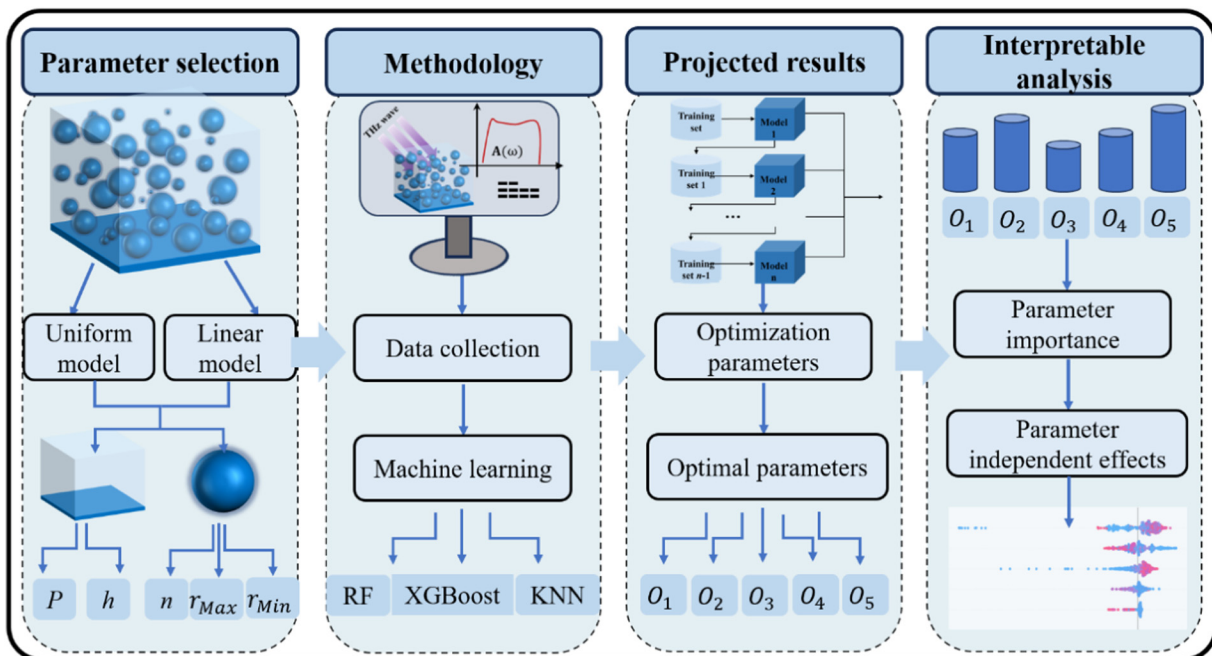

FIG. 1. The comprehensive process of utilizing machine learning for predicting spatially and frequency-selective optical field-coupled absorption in random metasurfaces.

number of spheres (n), the minimum radius (r_{Min}), and the maximum radius (r_{Max}) were selected as the structural parameters, respectively. In this work, a three-dimensional time-domain finite-difference method is used to calculate the optical properties and resonant behavior of the metasurface. Various details about the setup of the model construction can be obtained in SM1 in the supplementary material.

The machine learning process involves the stages of preparation, learning, and evaluation. In the preparation phase, raw data are gathered and transformed into a machine-learning-friendly format, with the selection of appropriate input feature parameters (P, h, n, r_{Max}, r_{Min} as identified in the previous paragraph). Subsequently, during the learning step, suitable machine learning algorithms are chosen for modeling.

During the learning phase, initial datasets are collected for the two models. The dataset used to train and test the machine learning models was generated through full-wave finite-difference time domain simulations of the random microsphere metasurface structures. Specifically, the structural parameters were sampled within the following ranges: period P (6–15 μm), thickness h (10–40 μm), number of microspheres n (30–200), minimum radius r_{Min} (0.01–1.00 μm), and maximum radius r_{Max} (1.5–4.0 μm). A random uniform sampling strategy was employed to ensure broad coverage and diversity across the design space. Details regarding the parameter ranges and minimum precision for the two models are available in Table S1 in the supplementary material.

To enhance the efficiency and relevance of model training, the dataset for each model (uniform and linear) was constructed by randomly sampling structural parameters from predefined ranges and calculating the corresponding absorption spectra. Samples with an average absorption of below 60% across the 1–10 THz frequency range were discarded. This threshold was chosen because such designs generally exhibit weak resonance behavior and limited practical applicability as THz absorbers, and including them would dilute the ability of the machine learning models to identify and optimize high-performance structures. Ultimately, 681 sets of data for the uniform model and 693 for the linear model were obtained as the initial datasets. This filtering step reduces noise from low-performance designs, improving model efficiency and interpretability. To verify that it does not introduce significant bias, we performed ablation experiments comparing models trained on the full dataset and the filtered dataset (Table S2 in the supplementary material). The results indicate that while models trained on the full dataset can capture general trends, models trained on the filtered dataset achieve higher prediction accuracy and more reliable identification of critical parameters for high-performance designs.

For the evaluation step, three machine learning algorithms—Random Forest (RF), Extreme Gradient Boosting (XGBoost), and K Nearest Neighbors (KNN)—are selected and compared. These algorithms have demonstrated effectiveness in designing various micro- and nanodevices with high accuracy.[31–34] Conceptual diagrams and detailed explanations about these algorithms are provided in SM3 in the supplementary material. Among them, RF is an integrated learning model comprising multiple decision trees, aiming to enhance prediction accuracy and stability. It is adept at handling high-dimensional feature samples, eliminating the need for dimensionality reduction processing and accurately assessing feature importance in regression problems. It was included due to its ensemble strategy, which reduces overfitting and provides interpretability through feature importance analysis. KNN regression, an instance-based learning method, identifies the K closest samples in the training set to predict the target value for a given sample. KNN serves as a simple instance-based baseline model that interpolates between nearby samples without assumptions about data distribution, allowing straightforward evaluation of local patterns. XGBoost, also based on decision tree generation, introduces a regularization term to control model complexity, preventing overfitting and outperforming traditional gradient boosted decision trees (GBDTs). XGBoost was chosen for its ability to efficiently handle high-dimensional tabular data, capture complex non-linear relationships, and maintain stable performance with moderate-sized datasets.

III. RESULTS AND DISCUSSION

To assess the accuracy of the prediction models quantitatively and differently, two commonly used evaluation metrics were employed in this study: the mean square error (MSE) and the coefficient of determination (R^2),

$$MSE = \frac{1}{n}\sum_{i=1}^{n}(\hat{y}_i - y_i)^2, \quad (2)$$

$$R^2 = 1 - \frac{\sum_{i=1}^{N}(y_i - \hat{y}_i)^2}{\sum_{i=1}^{N}(y_i - y_{im})^2}, \quad (3)$$

where $\hat{y}_i$ and y_i represent the predicted and measured values, respectively, and y_{im} is the mean of the measured values. The MSE reflects the variance between the predicted and measured quantities, with a smaller MSE, indicating a more accurate prediction. R^2 is a statistical measure indicating how accurately the given model predicts the measured results. A value closer to 1 for R^2 indicates a higher degree of agreement between the predicted and measured quantities.

The dataset was trained using different algorithmic models, and the hyperparameters of each algorithmic model were optimized through stochastic search to ensure optimal prediction performance. Subsequently, the test set was employed for testing, and the optimized regression models were utilized for predicting the most structural parameters.

Interpretable analyses of algorithms play a crucial role in comprehending the performance of machine learning models and elucidating the underlying physical information, thereby enhancing their credibility. In this study, we employ the interpretable method of Shapley additive interpretation (SHAP), which effectively captures the influence of feature parameters on prediction outcomes.

SHAP is an approach inspired by game theory that aims to explain the predictions of machine learning models. It can be used for both global interpretation and local interpretation by obtaining the Shapley values for a single sample.[35] For a single sample, the Shapley value is calculated as

$$\text{Shapley value}(i) = \sum_{S \subseteq N \setminus \{i\}} \frac{|S|(M - |S| - 1)!}{M!}[f_x(S \cup \{i\}) - f_x(S)], \quad (4)$$

TABLE I. Optimized values of hyperparameters for different machine learning algorithms in two metasurface models.

Algorithm	Hyperparameters	Range of values	Uniform model	Linear model
RF	n_estimators	10–200	90	161
	max_features	auto, sqrt, log2, None	log2	log2
	max_depth	1–20	8	11
	min_samples_split	2–20	3	4
	min_samples_leaf	1–20	15	9
XGBoost	learning_rate	0–1	0.11	0.21
	n_estimators	50–500	465	272
	max_depth	3–10	3	6
	min_child_weight	1–10	2	6
	subsample	0.5–1	0.9	0.9
KNN	n_neighbors	1–20	5	6
	weights	Uniform/distance	Uniform	Uniform
	p	1–5	1	1

where N is the set dimension M of all feature parameters, S is a subset of the N dimension, $f_x(S)$ is the output obtained using only the set of feature parameters S, and $f_x(S \cup)$ is the output by adding the parameter i feature parameter set intuitively. Essentially, the

characteristics of a specific sample's Shapley value can be interpreted as the contribution that leads its output value to deviate from the average of the outputs of all samples. The magnitude of the Shapley value indicates the degree to which the feature
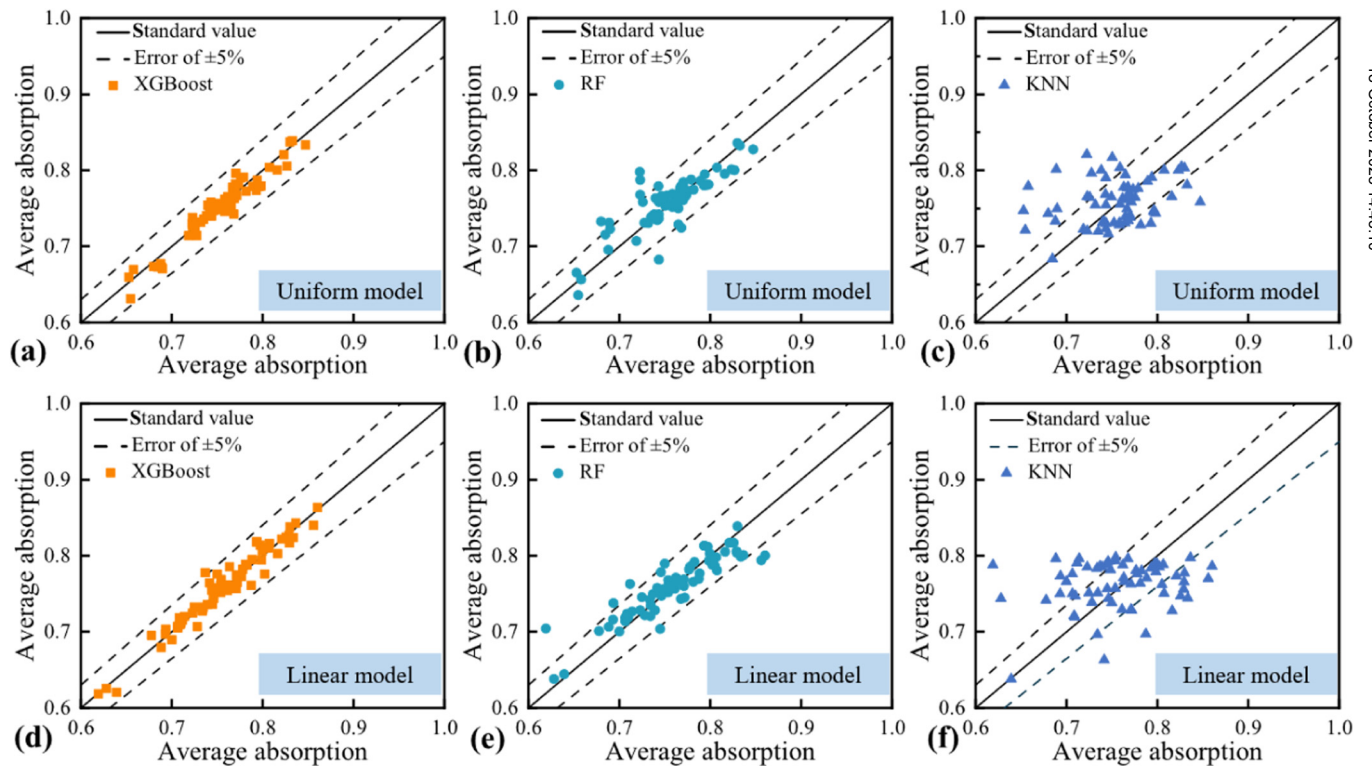
FIG. 2. Comparison of the average absorption in the 1–10 THz band for two metasurface models as estimated and measured by various machine learning algorithms. (a)–(c) Prediction of the true value for the uniform model using the XGBoost, RF, and KNN algorithms. (d)–(f) Predictions by the XGBoost, RF, and KNN algorithms for the true values of the linear model. The black dashed line represents the error bound of ±5%.
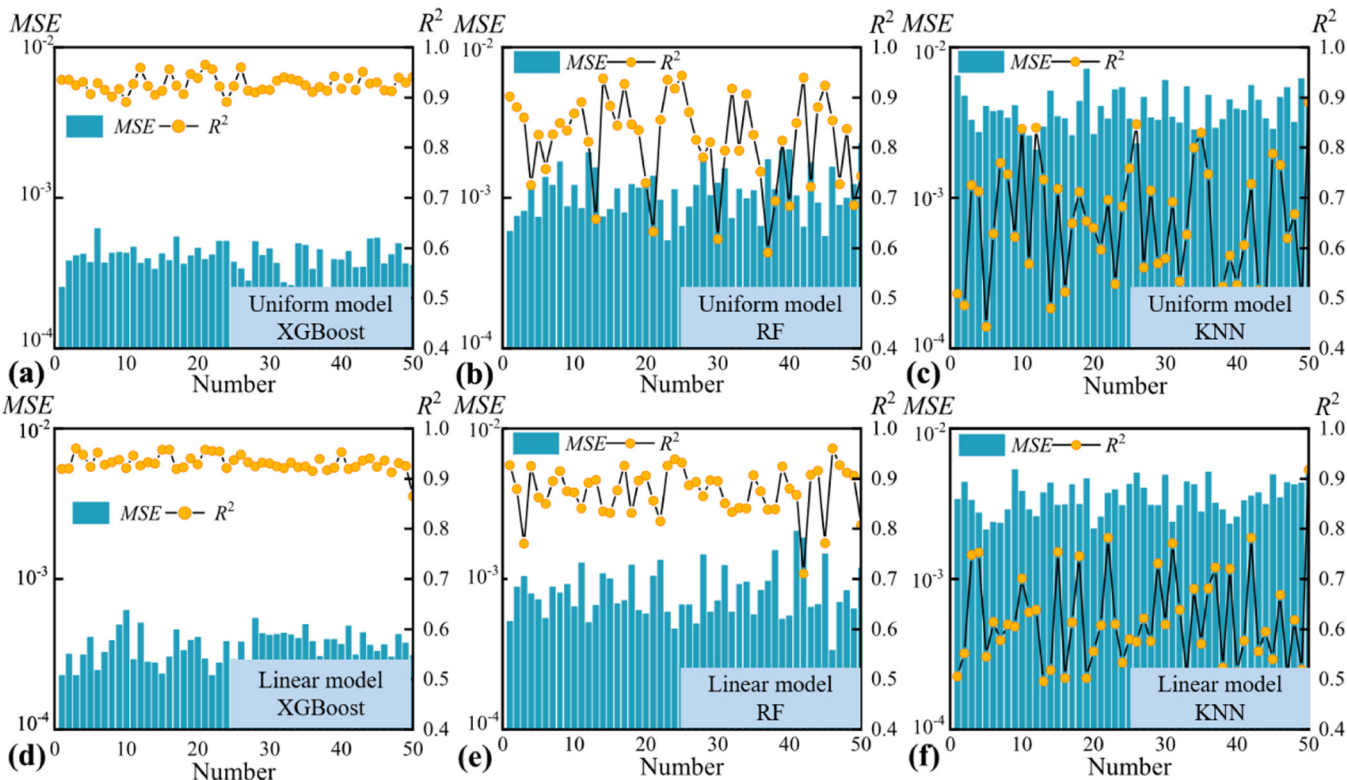
FIG. 3. Statistically obtained MSE and coefficient of R^2 for each algorithmic model after 50 repetitions. (a)–(c) Prediction of the true value for the uniform model using the XGBoost, RF, and KNN algorithms. (d)–(f) Predictions by the XGBoost, RF, and KNN algorithms for the true values of the linear model.

parameter contributes to the model prediction, and the sign of the Shapley value indicates whether the contribution is positive or negative. This represents the primary strength of the Shapley value, capturing both the magnitude of the influence of the feature in the sample and the positive or negative nature of the influence.

In this study, 90% of the collected datasets in both models were allocated to the training set, with the remaining 10% designated as the test set. The optimization of hyperparameters was performed using the random search method, and the optimal results are presented in Table I. Subsequently, the test set validation for

TABLE II. Optimized values for uniform and linear models obtained from different machine learning predictions.

	Uniform model			Linear model		
Algorithmic	XGBoost	RF	KNN	XGBoost	RF	KNN
P	9.8	9.8	8.4	8.8	9.3	10.1
H	25.1	20.3	21.7	30.2	30.4	29.3
N	68	96	85	82	86	65
r_{Min}	0.1	0.1	0.1	0.1	0.3	0.1
r_{Max}	2.5	2.4	2.5	2.5	2.2	2.4
Predicted value	87.14%	84.88%	84.01%	88.37%	87.45%	85.33%
True value	86.12%	78.12%	76.36%	87.82%	81.92%	76.24%
AE	1.02%	6.76%	7.65%	0.55%	5.53%	9.09%
RE	1.17%	7.96%	9.11%	0.62%	6.32%	10.65%

18 October 2025 14:43:10
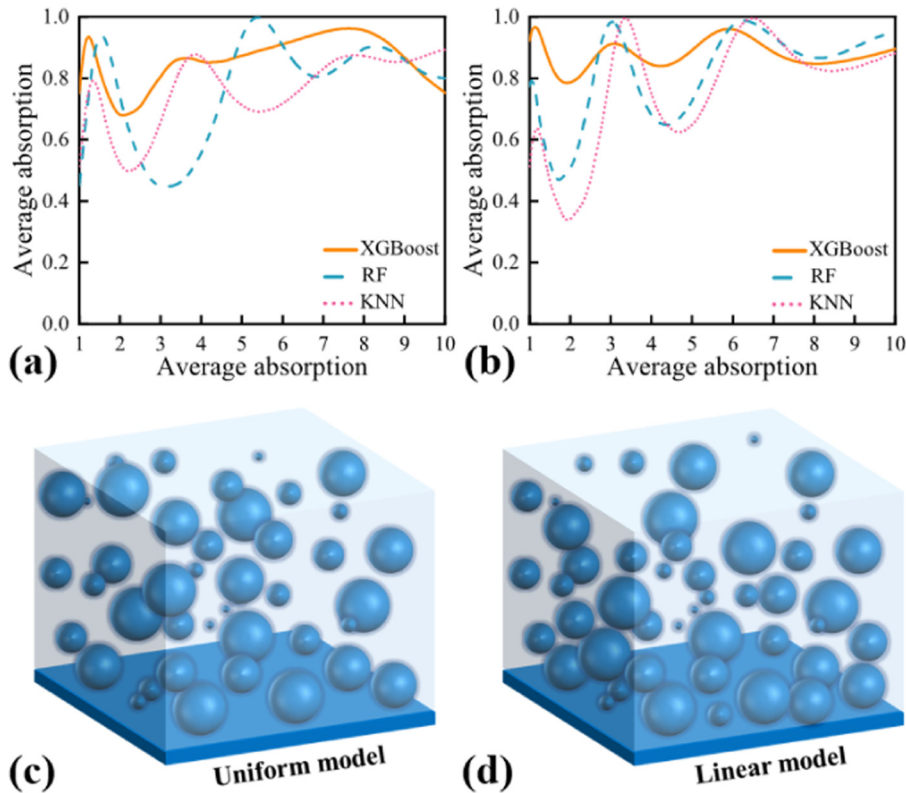
FIG. 4. Absorption spectra of the uniform and linear models obtained from different machine learning predictions and schematic representation of the models. (a) and (b) Predicted absorption spectra for uniform and linear models. (c) and (d) Schematic representation of the uniform metasurface model and the linear metasurface model.

both models was conducted, employing the various machine learning algorithms obtained from the optimization, enabling a comparative analysis of the predicted and true values, respectively.

For the uniform model, the three machine learning algorithms exhibited varying predictive capabilities, with XGBoost showing excellent predictive abilities as all predicted values were within a 5% error (Fig. 2). Conversely, for RF and KNN, 7 out of 68 and 20 out of 68 data points exceeded the 5% error, indicating a decrease in predictive ability compared to XGBoost. Similarly, for the linear model, 68 out of 69, 62 out of 69, and 36 out of 69 data points were within the 5% error boundaries for the three algorithms, showcasing comparable prediction performance to the uniform model.

To quantitatively compare the prediction accuracy of each parameter for different data points, the calculated absolute error (AE) and relative error (RE) for all data points are illustrated in Fig. S4 in the supplementary material. The predicted values of XGBoost exhibit smoother errors, with RE reaching 10% for only one data point. In contrast, the maximum RE of RF predictions reaches 30%, and KNN exceeds 40%. To further verify the generalizability of the models, we performed fivefold cross-validation separately for the uniform and linear metasurface models. The results for the uniform model show that XGBoost achieved an average R^2 of 0.925 ± 0.015, demonstrating both high accuracy and stability; RF exhibited a higher variance with $R^2 = 0.817 \pm 0.046$; KNN showed relatively lower performance with $R^2 = 0.618 \pm 0.058$.

For the linear model, XGBoost achieved an average R^2 of 0.932 ± 0.012, RF reached $R^2 = 0.872 \pm 0.031$, and KNN obtained $R^2 = 0.628 \pm 0.055$, indicating that the linear model generally leads to slightly higher predictive accuracy and stability across algorithms.

The learning curves (Fig. S5 in the supplementary material) show that XGBoost exhibits the highest training and validation R^2 across all training set sizes. With small datasets, XGBoost and RF exhibit larger gaps between training and test R^2, indicating some overfitting, but this gap narrows as the dataset size increases. KNN consistently shows lower R^2 values for training and test sets, suggesting underfitting. Overall, XGBoost demonstrates the best generalization performance, with training and test R^2 converging as the dataset size approaches the full 551 samples (<0.05), further supporting their generalizability despite the relatively limited dataset size.

Furthermore, considering the contingent nature of a single training of the model, 50 repetitions of each machine learning algorithm were conducted to verify its stability. The statistically obtained MSE and R^2 are shown in Fig. 3. The average values of MSE for the uniform model and the linear model for 50 repetitions of XGBoost are only 0.000 408 and 0.000 367, and the average R^2 reaches 0.927 and 0.932, demonstrating excellent fitting ability. For RF, the average values of MSE for the uniform model and linear model are 0.001 16 and 0.000 869, respectively, with average R^2 values of 0.816 and 0.874. In a single training, RF can reach a
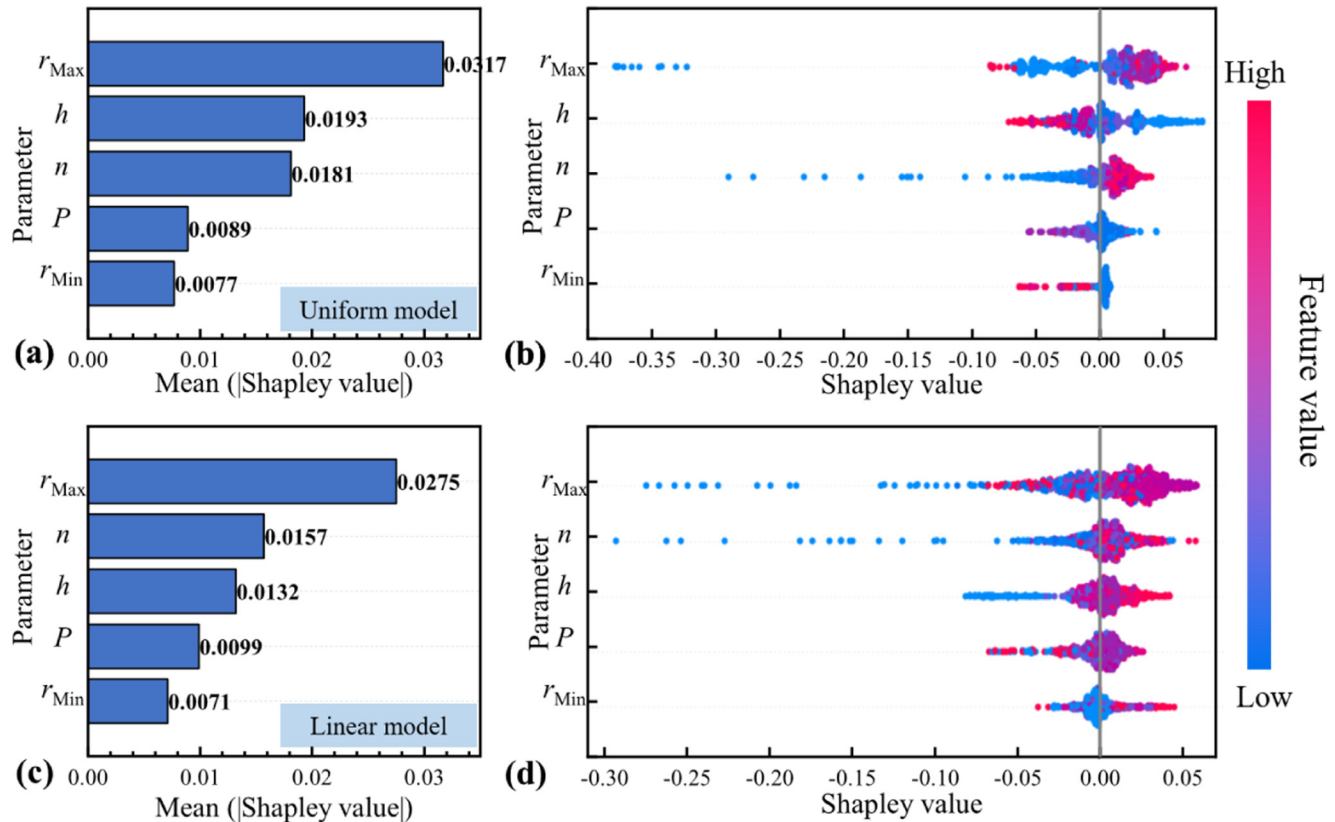
FIG. 5. Summary plots of the Shapley values of the uniform and linear models. (a) and (b) Mean Shapley values and plots depicting the distribution of Shapley values for each parameter in the uniform model. (c) and (d) Mean Shapley values and plots illustrating the distribution of Shapley values for each parameter in the linear model.

maximum R^2 of 0.961, but the results fluctuate considerably, and the average performance of RF is lower than that of XGBoost. In contrast, KNN shows poorer stability, with MSE averages of only 0.003 95 and 0.003 55 for the uniform and linear models, and average R^2 of only 0.620 and 0.648. It is worth noting that for all algorithms, the linear model exhibits higher prediction accuracy compared to the uniform model. This is because the linear distribution reduces the randomness of the microsphere distribution to some extent, thereby demonstrating higher stability.

The optimal parameters were predicted using the machine learning obtained from optimization for the uniform and linear models, respectively, and computationally validated against the output parameters. The structural parameters obtained are shown in Table II. The absorption spectra of these results obtained computationally are given in Fig. 4 and are schematically plotted for the uniform and linear models. Among them, XGBoost shows optimal prediction performance, achieving an average absorption of 86.12% and 87.82% for the uniform and linear models, respectively, with only 1.17% and 0.62% for the RE. Both average absorption and prediction accuracy are much better than RF (78.12% and 87.82%) and KNN (76.36% and 76.24%). Since XGBoost outperforms other

machine learning algorithms and is interpretable, the next interpretable analyses are based on the XGBoost model.

The SHAP summary plot effectively combines the importance of a feature with the effect of the feature (positive or negative) by summarizing a feature parameter and the corresponding Shapley value. In this study, the Shapley value indicates how much a given feature parameter changes the average absorption of a uniform or linear model.

Figure 5 provides a summary plot of SHAP for each structural parameter for both uniform and linear models. The average Shapley values for each structural parameter are initially given and sorted from largest to smallest along the y axis. Among all parameters, r_{Max} exhibits the greatest degree of influence. For the two models, r_{Max} has the widest distribution of Shapley values on the horizontal axis, ranging from -0.40 to 0.05 and -0.28 to 0.07, respectively. This is because the radius of the microspheres directly affects the frequency of the light–field coupling, and the range of r_{Max} determines the frequency range of the light–field coupling. The number of microspheres also significantly affects the average absorption of the two models (with the width of the distribution of Shapley values being -0.30 to 0.04 and -0.30 to 0.06, respectively),
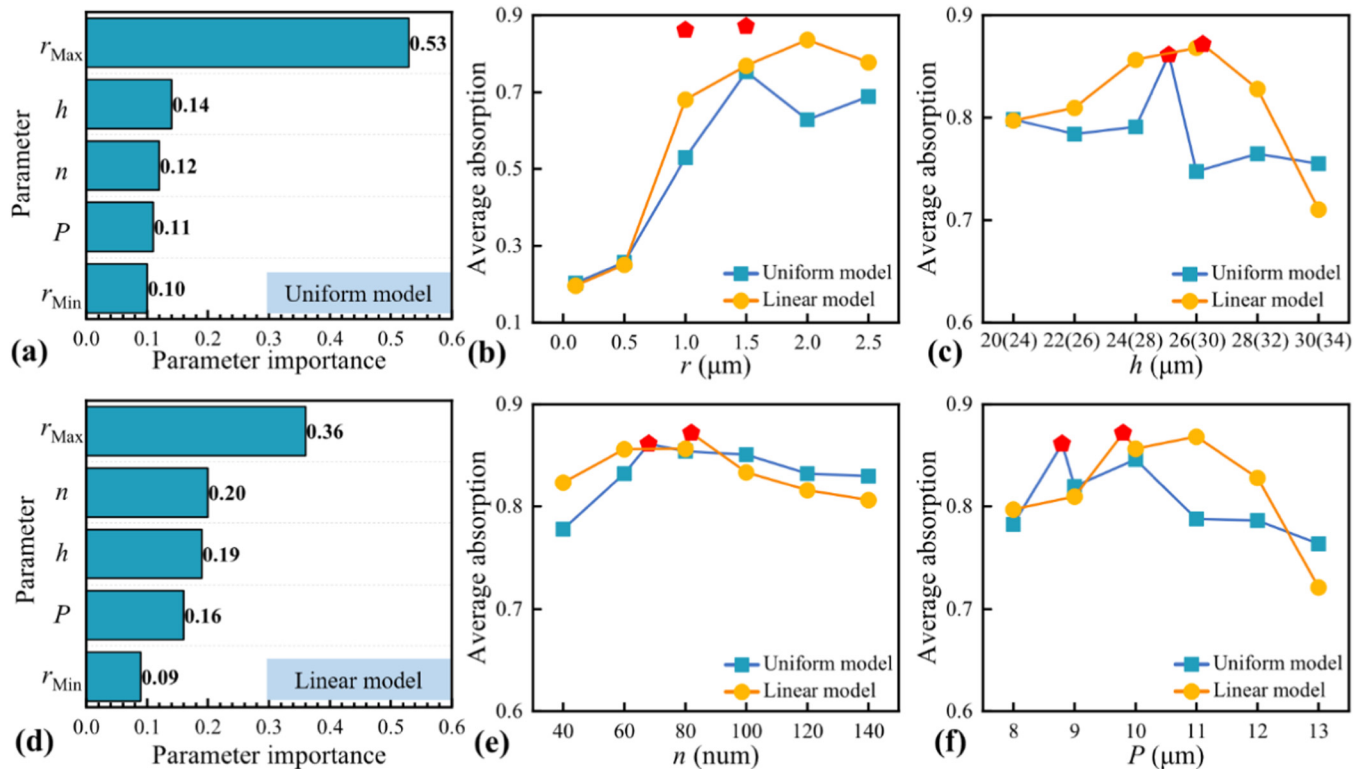
18 October 2025 14:43:10

FIG. 6. Summary plots of the parameters for the uniform and linear models. (a)–(c) Statistical results on the importance of different parameters in the uniform model and on the optical properties. (d)–(f) Statistical results on the importance of different parameters in the linear model and on the optical properties.

as n directly influences the strength of the light–field coupling inside the metasurface.

Additionally, Fig. 6 quantitatively calculates the importance of each feature parameter (with a total importance of 1) to validate the SHAP analysis in Fig. 5. The calculated results demonstrate high consistency with the SHAP summary plot (the importance share of r_{Max} reaches 0.53 and 0.36, respectively). To further validate the optimal values of each structural parameter, the absorption spectra of the uniform model and the linear model were separately calculated at different values, as shown in SM5 in the supplementary material.

The absorption spectra at different r were initially analyzed by fixing r to the same value for all microspheres and keeping all other parameters of the metasurface model constant for the calculations. It is worth noting that when r reaches $1.5\,\mu m$, the metasurface model can no longer accommodate the original number of n (68 and 82) internally. The maximum n accommodated by the two models at 1.5, 2.0, and $2.5\,\mu m$, are 75, 43, and 22 for the uniform model and 65, 35, and 19 for the linear model, respectively. Figure S6 in the supplementary material shows that overall absorption is low at r less than $1.0\,\mu m$ and higher absorption is first obtained at high frequencies as r gradually increases. As r further increases, the absorption peak gradually shifts to lower frequencies,

indicating that r is a crucial factor affecting the coupling frequency of the optical field, and different sizes of micrometer spheres correspond to the coupling of the optical field at different frequencies.

The absorption spectra of the two models at different n, h, and P were subsequently analyzed sequentially (Figs. S7–S9 in the supplementary material). The absorption is lower at lower n, when the light–field coupling strength is lower, and the spectra do not change significantly after n exceeds 60. For h and P, the effects are more similar, with both having a greater impact on absorption in the low-frequency bands, especially for larger values.

Figures 6(b), 6(c), 6(e), and 6(f) visualize the average absorption for different parameter values, with the red pentagrams indicating the optimal structural parameters obtained from the XGBoost predictions. All the values taken are within the optimal interval, demonstrating the accuracy of XGBoost in fitting and predicting the data. Moreover, during parameter variation, the average absorption of the two models corresponding to r_{Max} changes the most, consistent with the previous SHAP analysis.

During the dissipation of electromagnetic waves, intricate optical field coupling processes occur. Four resonance peaks (1.15, 3.61, 6.93, and 9.81 THz) were sequentially selected from low to high frequencies, and the electric field distribution in the x–y plane was analyzed (Fig. 7). In the spatial and frequency distribution of
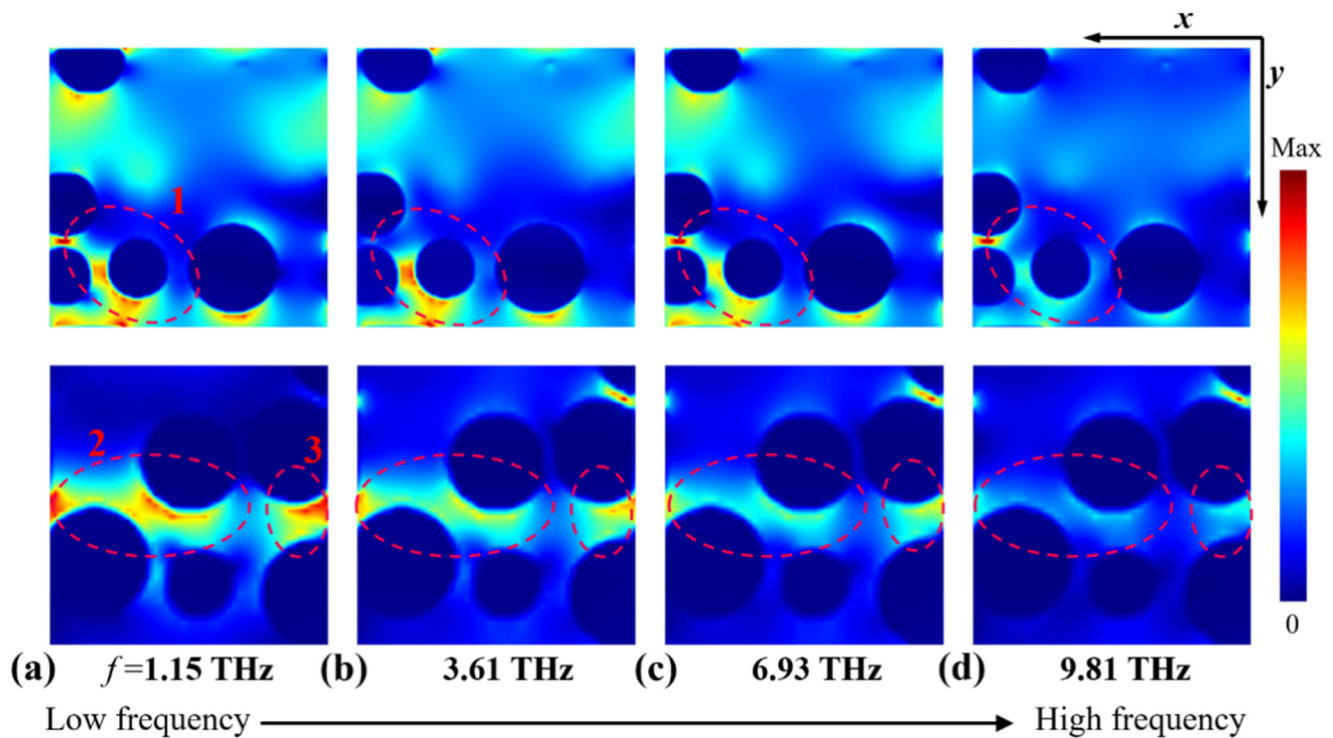
FIG. 7. The distributions of electric fields in frequency and spatial domains were computed for both models. (a)–(d) 1.15, 3.61, 6.93, and 9.81 THz.

the electric field, strong electric field confinement is observable around or near the nanosphere when polarized incidence is in the x direction, suggesting the particles produce a localized surface plasmon resonance.[36,37] A notable evolution of the electric field with frequency is apparent, as indicated by the red dashed line in Fig. 7.

In the low-frequency band, significant strong plasma coupling effects from the excitation of neighboring particles are observed. As the frequency increases, the resonance mode between microparticles transforms from strong plasma near-field coupling of neighboring resonators to strong local plasma excitation of a single resonator.

In addition to considering the electric field distribution in the x–y plane, the intrinsic evolution characteristics of the electric field in the x–z plane and y–z plane are also investigated, as shown in SM6 in the supplementary material. In both the uniform and linear models (Figs. S10 and S11 in the supplementary material), besides being able to observe the transition between plasma near-field coupling and local plasma resonance (Figs. S2, S5, and S7 in the supplementary material), it is also possible to observe the transition process of the resonance region progressively moving from the bottom of the metasurface to the top of the surface as the frequency is increased (Figs. S1, S3, S4, and S6 in the supplementary material), where labeled region S6 appears to have a resonance intensity that first increases and then decreases. The study of these distribution characteristics confirms that the random distribution

of particles can achieve spatial and frequency-selective absorption, providing a new idea for large broadband absorption in the THz band.

Due to the complex incidence conditions involved in the real working environment, it is necessary to study the optical performance at different THz wave incidences. The absorption performances of the two models at incidences with different polarization angles are discussed, as shown in Figs. 8(a) and 8(d). During the variation in the THz wave polarization angle, overall excellent optical performance (average absorption greater than 80%) is maintained despite a certain degree of change in the absorption behavior, indicating that this randomly distributed metasurface has a certain degree of polarization-insensitive properties. At tilted incidences of THz waves, high absorption is still maintained over the entire spectral range as the incidence angle is increased to 60°, attributed to the co-resonance of the randomly distributed micrometer spheres inside the model. This also confirms the ability of the random metasurface obtained by the XGBoost design to cope with complex electromagnetic environments.

To benchmark the performance of the proposed metasurfaces, we compared our results with recent THz absorbers reported in the literature (Table III).[38–40] Graphene-based absorbers and multilayer designs have demonstrated absorption efficiencies ranging from 88% to 99% within targeted frequency bands. Although these designs can achieve higher peak absorption, they often require complex multilayer fabrication or precise nanoscale patterning. In
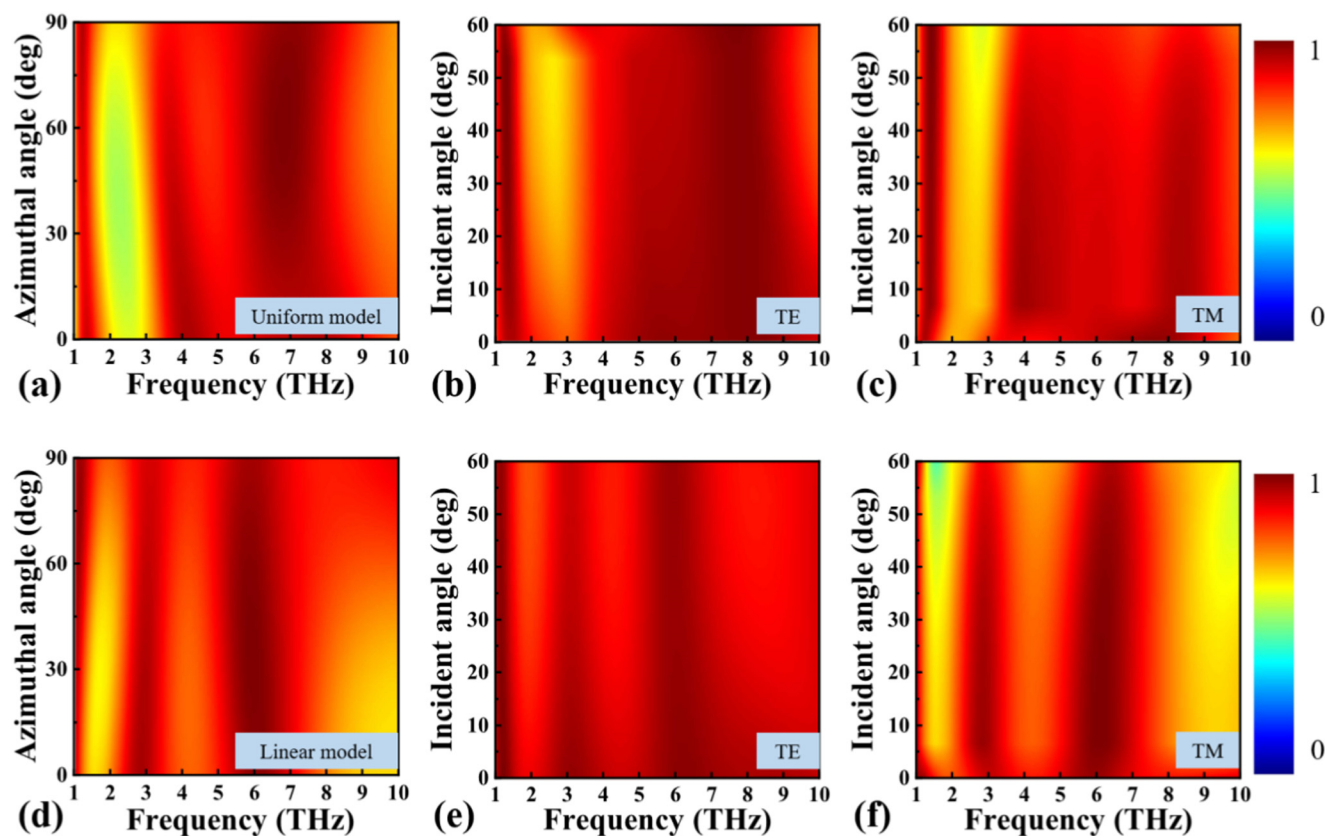
FIG. 8. Absorption behavior of two models for different polarization states and incidence angles. (a)–(c) Uniform model. (d)–(f) Linear model.

contrast, the random microsphere metasurfaces proposed here achieve high average absorptions of 86.12% and 87.82% across the 1–10 THz band, providing competitive performance with simpler fabrication and greater design flexibility. This underscores the practical advantage of our approach for efficient broadband THz absorption.

To interpret the high-dimensional machine learning models for random metasurfaces, we applied SHAP to quantify the contribution of each structural parameter to THz absorption. Unlike previous studies that primarily use SHAP

to engineer new features or identify strong interactions,[41] our approach explicitly correlates the SHAP-derived feature importance with the physical behavior of the metasurface. For example, the radius of microspheres and the number of spheres are identified as the dominant contributors, consistent with electric field simulations of resonance patterns. This approach not only ranks parameter importance but also validates the underlying physical mechanism, enabling efficient and interpretable optimization of high-performance random metasurfaces.

TABLE III. Comparison of the proposed metasurface with previously published metasurfaces.

Reference	Absorption range (THz)	Absorption (%)	Structure type
38	1.12–3.78	>90	Three-layer graphene metasurface
39	1.93–4.61	>90	Composite metasurface
	1.45–3.87	>90	Composite metasurface
40	4.07–9.00	>90	Graphene metasurface
This work (uniform model)	1.00–10.00	86.12%	Random microsphere metasurface
This work (linear model)	1.00–10.00	87.82%	Random microsphere metasurface

18 October 2025 14:43:10

IV. CONCLUSIONS

In conclusion, this paper presents the design of two THz broadband absorbing metasurfaces composed of random microspheres, showcasing frequency and spatial selective absorption, facilitated by machine learning. High-performance machine learning models are established for rapid parameter optimization, achieving R^2 values of 0.927 and 0.932, and MSE values of only 0.000 408 and 0.000 367, respectively, indicating a high degree of predictive ability. Both the uniform and linear models, derived from the optimization process, demonstrate outstanding optical performance in the 1–10 THz band. The absorption behavior is interpretable through machine learning analysis and validated by studying the physical mechanism. These results underscore that random metasurfaces designed by machine learning can effectively achieve large-bandwidth THz wave absorption, with potential applications in diverse fields, including military stealth and nondestructive testing.

SUPPLEMENTARY MATERIAL

See the supplementary material for detailed parameter settings for simulation, the algorithm parameter selection, conceptual diagrams and explanations of machine learning algorithms, comparison of parameter predictions, learning curves of different algorithms, absorption spectra at different structural parameters, and electric field distributions in the x–z and y–z planes.

ACKNOWLEDGMENTS

AUTHOR DECLARATIONS

Conflict of Interest

The authors have no conflicts to disclose.

Author Contributions

Meng Xu: Conceptualization (equal); Data curation (equal); Formal analysis (equal); Funding acquisition (equal); Writing – original draft (equal). **Zhipeng Ding:** Data curation (equal); Formal analysis (equal). **Wei Su:** Conceptualization (equal); Funding acquisition (equal); Supervision (equal); Writing – review & editing (equal). **Bin Tang:** Conceptualization (supporting); Software (supporting). **Hongbing Yao:** Funding acquisition (equal); Supervision (equal); Writing – review & editing (equal).

DATA AVAILABILITY

The data that support the findings of this study are available within the article and its supplementary material.

REFERENCES

[1] R.-H. Fan, Y. Zhou, X.-P. Ren, R.-W. Peng, S.-C. Jiang, D.-H. Xu, X. Xiong, X.-R. Huang, and M. Wang, Adv. Mater. **27**(7), 1201–1206 (2015).

[2] X. Cai, A. B. Sushkov, R. J. Suess, M. M. Jadidi, G. S. Jenkins, L. O. Nyakiti, R. L. Myers-Ward, S. Li, J. Yan, D. K. Gaskill, T. E. Murphy, H. D. Drew, and M. S. Fuhrer, Nat. Nanotechnol. **9**(10), 814–819 (2014).

[3] Y. Zheng, A. Maekawa, and Y. Monnai, APL Photonics **10**(7), 076105 (2025).

[4] M. Fu, N. Xia, Y. Duan, F. Zhou, and Y. Li, AIP Adv. **14**(2), 025210 (2024).

[5] Z. Ding, W. Su, H. Lu, H. Wu, and H. Yao, Opt. Laser Technol. **163**, 109446 (2023).

[6] S. Taravati and G. V. Eleftheriades, ACS Photonics **9**(2), 305–318 (2022).

[7] J. Ma, Y.-Y. Zhang, H. Liu, G.-M. Chen, Y. Li, H. Zhang, Y.-X. Fan, and Z.-Y. Tao, J. Appl. Phys. **137**(9), 093101 (2025).

[8] Y. Cheng, R. Xing, F. Chen, H. Luo, A. A. Fathnan, and H. Wakatsuchi, Adv. Photonics Res. **5**(8), 2300303 (2024).

[9] Z. Huang, Z. Wang, Y. Cheng, X. Li, J. Wang, L. Zhou, H. Xu, X. Luo, and L. Chen, Sci. China: Phys., Mech. Astron. **68**(7), 274201 (2025).

[10] C. Rong, L. Wu, J. Tao, Y. Cheng, K. Wang, L. Chen, H. Luo, F. Chen, and X. Li, J. Lightwave Technol. **43**(18), 8538–8562 (2025).

[11] Y. Zhang, Y. Liu, Y. Wang, S. Zheng, X. Hao, M. Liu, and H. Zhang, J. Appl. Phys. **137**(5), 053102 (2025).

[12] Z. Ding, W. Su, Y. Luo, L. Ye, W. Li, Y. Zhou, B. Tang, and H. Yao, Mater. Des. **234**, 112331 (2023).

[13] X. You, R. T. Ako, S. Sriram, and W. Withayachumnankul, Laser Photonics Rev. **19**(7), 2401011 (2025).

[14] Z. Huang, Y. Zheng, J. Li, Y. Cheng, J. Wang, Z.-K. Zhou, and L. Chen, Nano Lett. **23**(23), 10991–10997 (2023).

[15] K. Zhang, S. Dong, X. Wu, K. Yu, and Y. Liu, Opt. Laser Technol. **180**, 111490 (2025).

[16] R. Ali, W. Su, M. Ali, A. Akhtar, S. Sadaf, J. Yue, and H. Wu, J. Appl. Phys. **138**(4), 043101 (2025).

[17] L. Wu, L. Yang, B. Cai, Y. Cheng, and Z. Cheng, Physica B **708**, 417205 (2025).

[18] N. I. Landy, S. Sajuyigbe, J. J. Mock, D. R. Smith, and W. J. Padilla, Phys. Rev. Lett. **100**(20), 207402 (2008).

[19] Z. Ding, W. Su, Y. Luo, L. Ye, W. Li, Y. Zhou, J. Zou, B. Tang, and H. Yao, Nanoscale **16**(3), 1384–1393 (2024).

[20] Y. Cui, J. Xu, K. H. Fung, Y. Jin, A. Kumar, S. He, and N. Fang, Appl. Phys. Lett. **99**, 253101 (2011).

[21] M. Shahnawaz, H. B. Baskey, and J. A. M, J. Appl. Phys. **137**(24), 243104 (2025).

[22] X. Liu, Y. Xie, J. Qiu, W. Chen, Y. Liu, and J. Zhu, Nanophotonics **12**(23), 4319–4328 (2023).

[23] Y. M. Qing, H. F. Ma, and T. J. Cui, Opt. Express **26**(25), 32442–32450 (2018).

[24] G. Li, AIP Adv. **15**(7), 075113 (2025).

[25] Z. Li, R. Pestourie, Z. Lin, S. G. Johnson, and F. Capasso, ACS Photonics **9**(7), 2178–2192 (2022).

[26] S. So, T. Badloe, J. Noh, J. Bravo-Abad, and J. Rho, Nanophotonics **9**(5), 1041–1057 (2020).

[27] A. Ueno, J. Hu, and S. An, npj Nanophotonics **1**(1), 36 (2024).

[28] P. D. Cunningham, N. N. Valdes, F. A. Vallejo, L. M. Hayden, B. Polishak, X.-H. Zhou, J. Luo, A. K.-Y. Jen, J. C. Williams, and R. J. Twieg, J. Appl. Phys. **109**(4), 043505 (2011).

[29] Z. Chen, J. Chen, H. Tang, T. Shen, and H. Zhang, Opt. Express **30**(5), 6778–6785 (2022).

[30] L. Huang, G. Hu, C. Deng, Y. Zhu, B. Yun, R. Zhang, and Y. Cui, Opt. Express **26**(22), 29192–29202 (2018).

[31] L. Ye, W. Su, J. Zou, Z. Ding, Y. Luo, W. Li, Y. Zhou, H. Wu, and H. Yao, Opt. Laser Technol. **170**, 110208 (2024).

[32] H. Li, J. Lin, X. Lei, and T. Wei, Mater. Today Commun. **30**, 103117 (2022).

[33] S. Qian, X. Qiao, W. Zhang, Z. Yu, S. Dong, and J. Feng, Water Res. **249**, 121001 (2024).

[34]Z. Ding, W. Su, Y. Luo, L. Ye, H. Wu, and H. Yao, J. Mater. Chem. C **11**(17), 5625–5633 (2023).

[35]S. M. Lundberg and S.-I. Lee, Adv. Neural Inf. Process. Syst. **30**, 4768–4777 (2017).

[36]F. Le, D. W. Brandl, Y. A. Urzhumov, H. Wang, J. Kundu, N. J. Halas, J. Aizpurua, and P. Nordlander, ACS Nano **2**(4), 707–718 (2008).

[37]Z. Liu, G. Liu, X. Liu, J. Chen, and C. Tang, Opt. Lett. **48**(7), 1586–1589 (2023).

[38]L. Liu, W. Liu, and Z. Song, J. Appl. Phys. **128**(9), 093104 (2020).

[39]Z. Ding, W. Su, Y. Luo, L. Ye, H. Wu, and H. Yao, Mater. Des. **233**, 112215 (2023).

[40]M. Shahnawaz, H. B. Baskey, and M. J. Akhtar, Diamond Relat. Mater. **149**, 111598 (2024).

[41]A. Amini, A. Moshiri, M. A. C. Zadeh, and V. Nayyeri, Sci. Rep. **15**(1), 24029 (2025).

18 October 2025 14:43:10

Supplementary Material for:

Machine learning-based prediction of spatially and frequency-selective optical field coupled absorption in random metasurfaces

Meng Xu[1,2], Zhipeng Ding[1], Wei Su[1,a)], Bin Tang[3], and Hongbing Yao[1,a)]

[1]College of Mechanics and Engineering Sciences, Hohai University, Nanjing 211100, China

[2]Key Laboratory of Quantum Materials and Devices of Ministry of Education, School of Physics, Southeast University, Nanjing 211189, China

[3]School of Microelectronics and Control Engineering, Changzhou University, Changzhou 213164, China

Authors to whom correspondence should be addressed: opticsu@hhu.edu.cn, alenyao@hhu.edu.cn.

Contents

SM1: Detailed parameter settings for simulation

In this study, periodic boundary conditions are employed in both the x- and y-directions for both the uniform and linear models, with a perfect matching layer (PML) set in the z-direction for numerical solutions. The THz incident band spans from 1.0 to 10.0 THz, and the mesh precision is set to 5, with additional mesh layers added to the entire metasurface to ensure simulation accuracy. The incident wave is vertically oriented along the negative z-axis, and two monitors are positioned above the light source and at the bottom of the metasurface to acquire the reflection $R(\omega)$ and transmission $T(\omega)$ spectra. The absorption $A(\omega)$ can be calculated using the expression $A(\omega) = 1 - R(\omega) - T(\omega)$. Given that the bottom Ag substrate (0.5 µm) effectively prevents the incident wave from penetrating, $R(\omega)$ tends to 0, further simplifying the absorption expression to $A(\omega) = 1 - R(\omega)$.

SM2: Algorithm parameter selection

TABLE S1. The range of values and minimum accuracy of the structural parameters of the two models.

| Parameter	Uniform model		Linear model	
	Range (µm)	Minimum accuracy (µm)	Range (µm)	Minimum accuracy (µm)
P	6.0-15.0	0.1	6.0-15.0	0.1
h	10.0-40.0	0.1	10.0-40.0	0.1
n	30-200	1	30-200	1
r_{Max}	1.5-4.0	0.1	1.5-4.0	0.1
r_{Min}	0.01-1.00	0.01	0.01-1.00	0.01

TABLE S2. Performance comparison of models trained on full vs. filtered datasets

Algorithm	Dataset	Uniform Model	Linear Model
XGBoost	Full dataset	0.891	0.897
XGBoost	Filtered dataset	0.925	0.932
RF	Full dataset	0.801	0.845
RF	Filtered dataset	0.817	0.872
KNN	Full dataset	0.582	0.605
KNN	Filtered dataset	0.618	0.628

SM3: Conceptual diagrams and explanations of machine learning algorithms

(1) RF

The RF regression model comprises multiple regression trees, and there is no correlation between each decision tree in the forest. The final output of the model is collectively determined by each decision tree in the forest. Randomness in the RF is evident in two aspects: first, in sample randomness, as a certain number of samples are randomly extracted from the training set to form the root node samples of each regression tree; second, in feature randomness, as a certain number of candidate features are randomly selected when establishing each regression tree. The most suitable features are then chosen as split nodes. The schematic diagram of the entire algorithm is presented in Fig. S1:
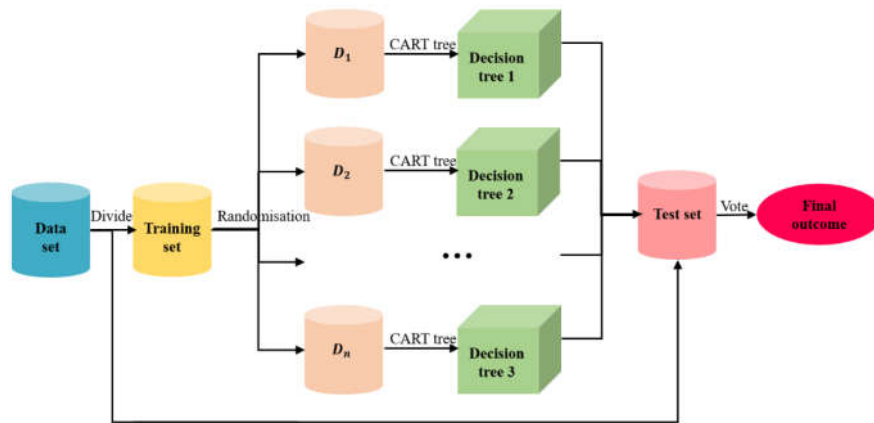
FIG. S1. Simplified conceptual diagram of RF model.

(1) Randomly draw sample points from the training sample set to create n new individual training sets (D_1, D_2.... D_n).

(2) Train a CART regression tree (decision tree) with each sub-training set. During the training process, the cutoff rule for each node involves randomly selecting k features from all the features. Then, the optimal cutoff point is chosen from the k features to perform left and right sub-tree divisions.

(3) Multiple CART regression tree models are generated through the second step.

(4) The final prediction of each CART regression tree is the mean of the leaf nodes reached by that sample point.

(5) The final prediction of the RF is the mean of the predictions of all CART regression trees.

In the RF algorithm model, the primary influential hyperparameters include *n_estimators* (the number of iterations for model training), *max_features* (the number of features), *max_depth* (the maximum depth of the tree, affecting the fitting ability), *min_samples_split* (the minimum number of samples required to split internal nodes), and *min_samples_leaf* (the minimum number of samples required at leaf nodes).

(2) XGBoost
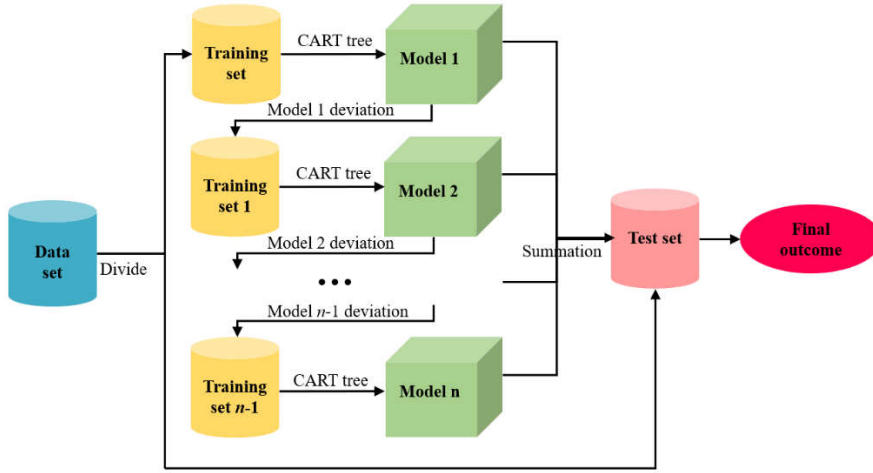
FIG. S2. Simplified conceptual diagram of XGBoost model.

The objective function of XGBoost comprises a loss function and a regularization term, assessing the fit and complexity of the data, respectively. Fig. S2 presents a schematic of XGBoost constructing multiple decision trees, where each decision tree is fitted to the residuals of the preceding one:

$$\hat{y}_i^{(n)} = y_i + \eta f_n(x_i) \tag{S1}$$

where $\hat{y}_i^{(n)}$ is the sum of the previously predicted values of the nth tree, $f_n(x_i)$ is the predicted value of the *n*-th tree, and η is the approximation coefficient of the new spanning tree model. In the XGBoost algorithm model, the principal influential hyperparameters include *learning_rate* (speed of learning), *n_estimators* (number of iterations for model training), *min_child_weight* (sum of sample weights of the smallest leaf nodes), *max_depth* (the maximum depth of the tree), and *subsample* (proportion of sample).

(3) KNN

KNN is an instance-based learning method, as illustrated in Fig. S3: for a given observational sample, identify the K nearest samples in the training set and employ their average to predict the target value of that sample. The nearest samples are depicted for K values of 1, 3, and 10, respectively. It is well-suited for regression problems and serves as a simple and user-friendly machine learning algorithm. The prediction of KNN regression is associated with the target value of the sample closest to that particular sample, making the method locally linear in the data space. In the KNN algorithm model, the primary influential hyperparameters encompass $n\_estimators$ (number of iterations for model training), *weights* (weights of the nearest neighbor samples of each sample), and p (p-value of the Minkowski distance).
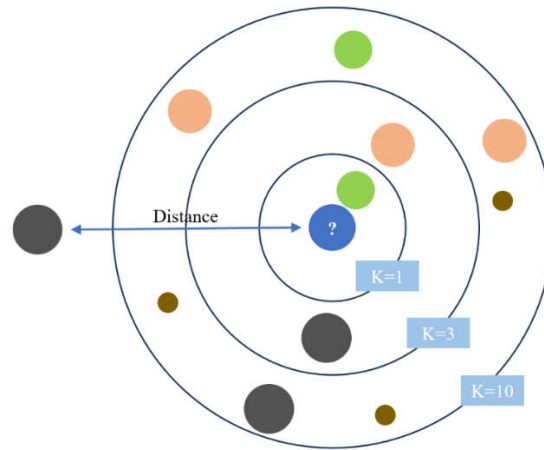
FIG. S3. Simplified conceptual diagram of KNN model.

SM4: Comparison of parameter predictions
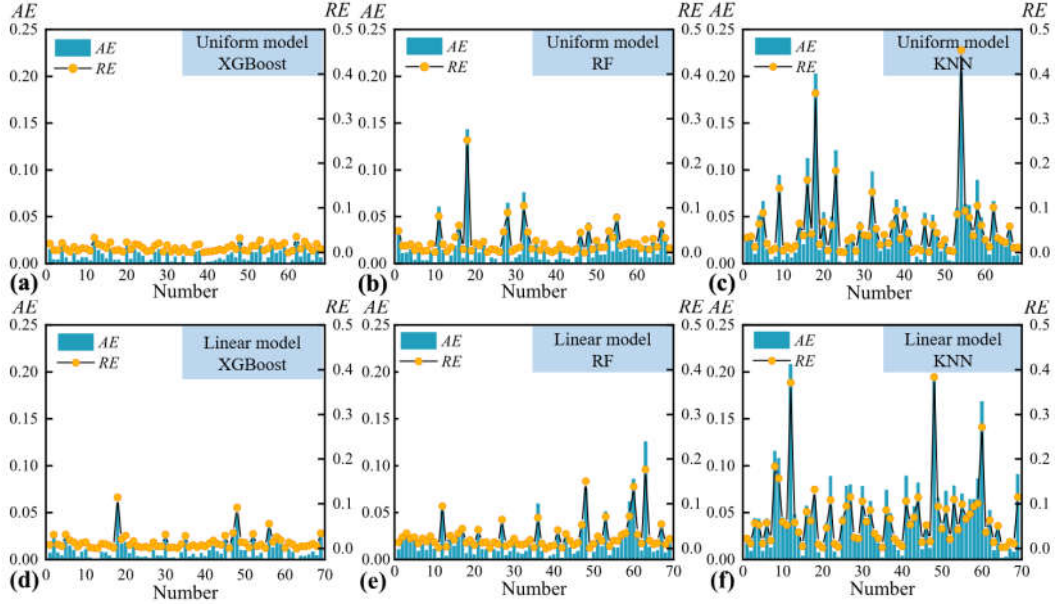
FIG. S4. Comparison of the average absorption achieved by various machine learning algorithms for two metasurface models. (a-c) Prediction of true values for the uniform model by the XGBoost, RF, and KNN algorithms. (d-f) Predictions of true values for the linear model by the XGBoost, RF, and KNN algorithms.

SM5: Learning curves of different algorithms
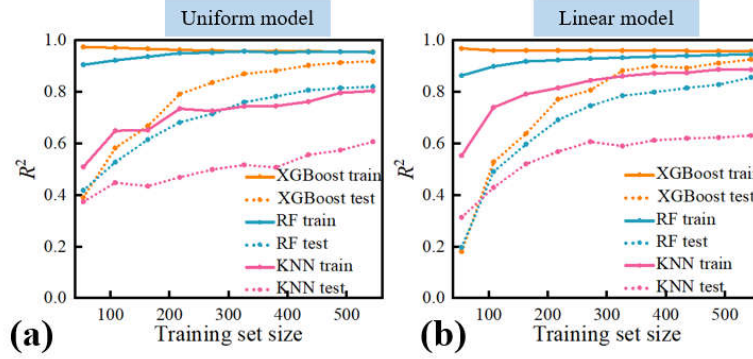
FIG. S5. Learning curves of different algorithms at varying training set sizes. (a) Uniform model. (b) Linear model.

SM6: Absorption spectra at different structural parameters
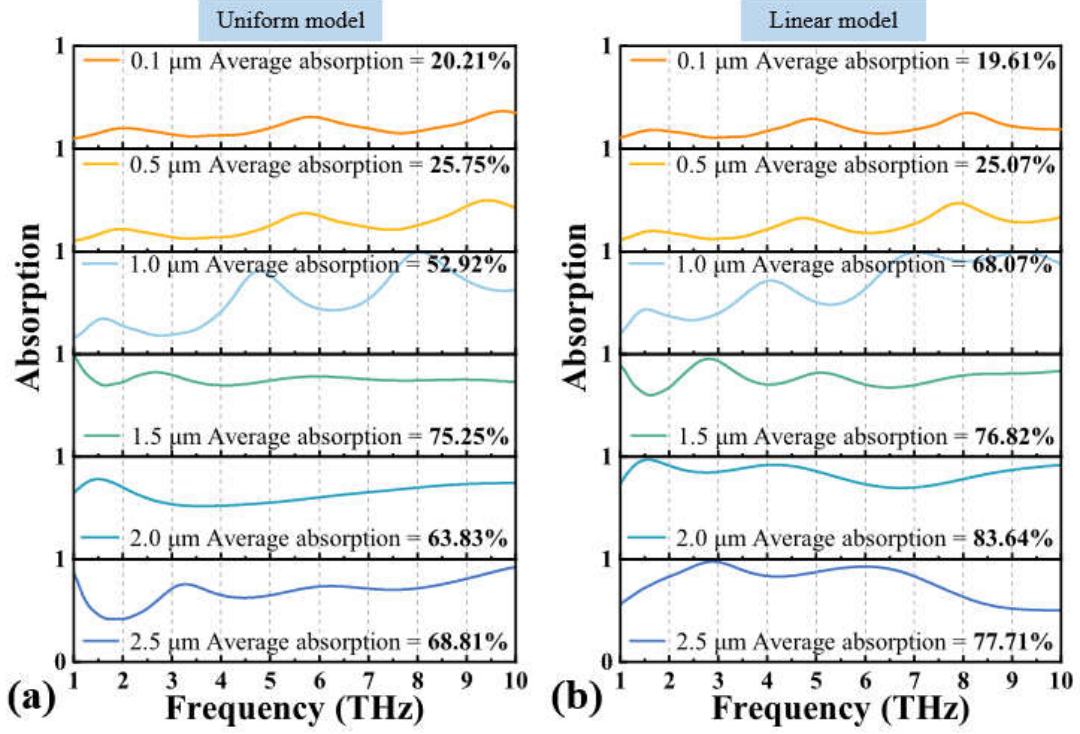
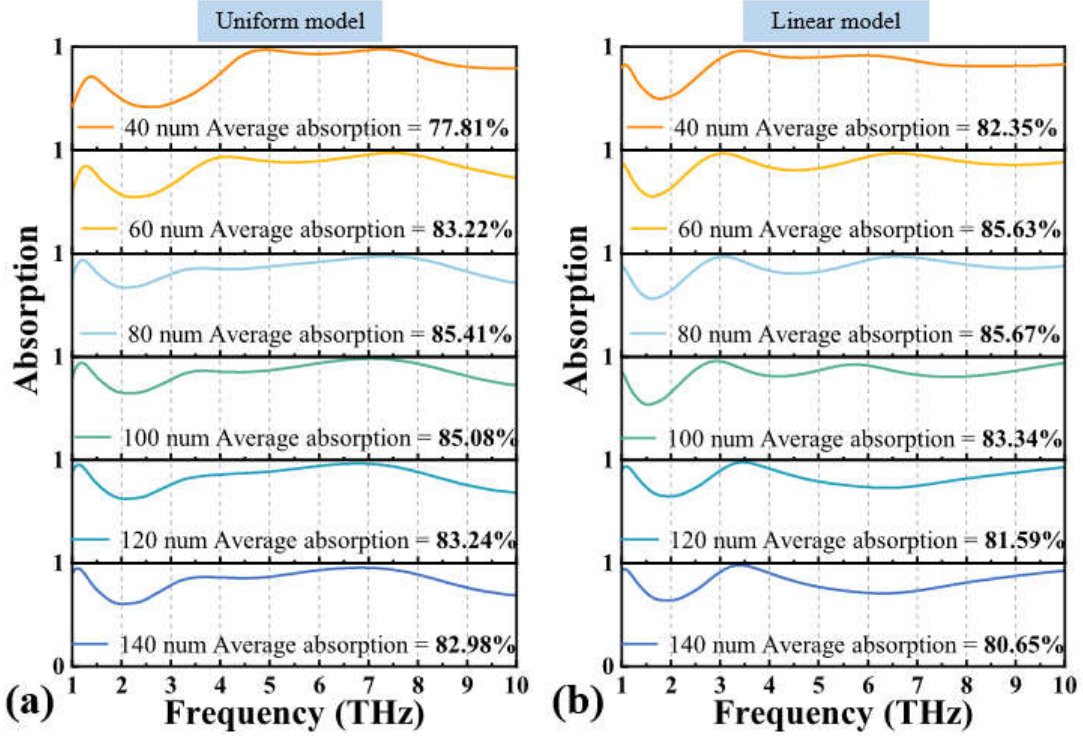**FIG. S6.** Absorption spectra of the two models at different *r*. (a) Uniform model. (b) Linear model.

FIG. S7. Absorption spectra of the two models at different *n*. (a) Uniform model. (b) Linear model.
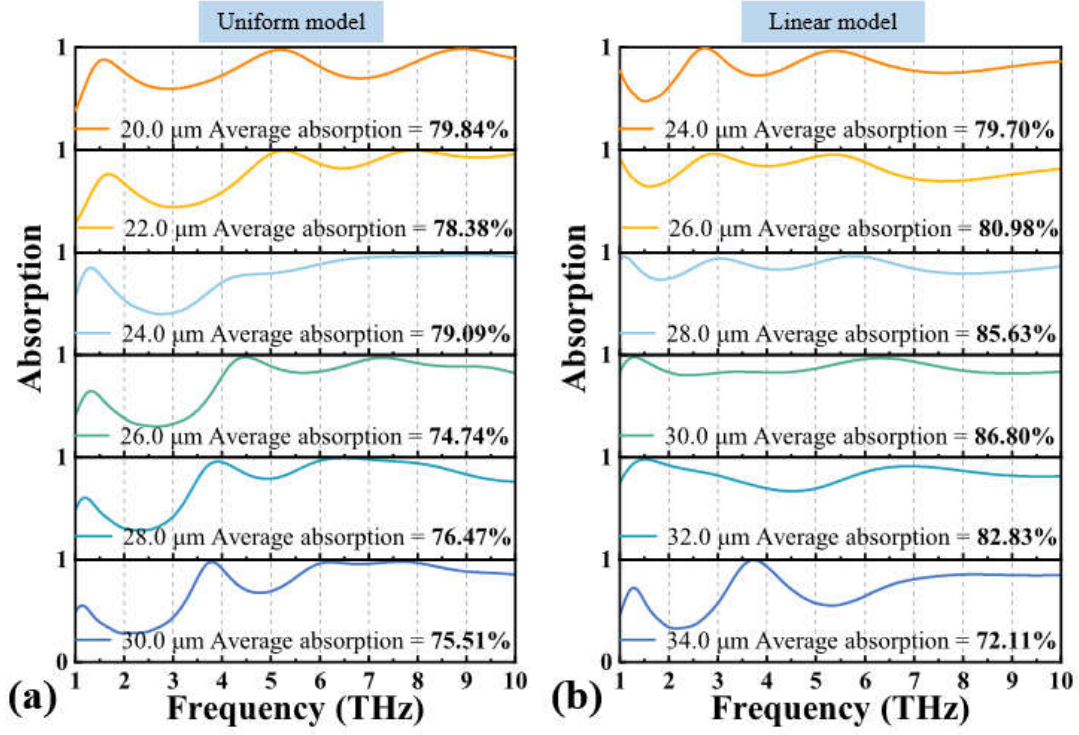
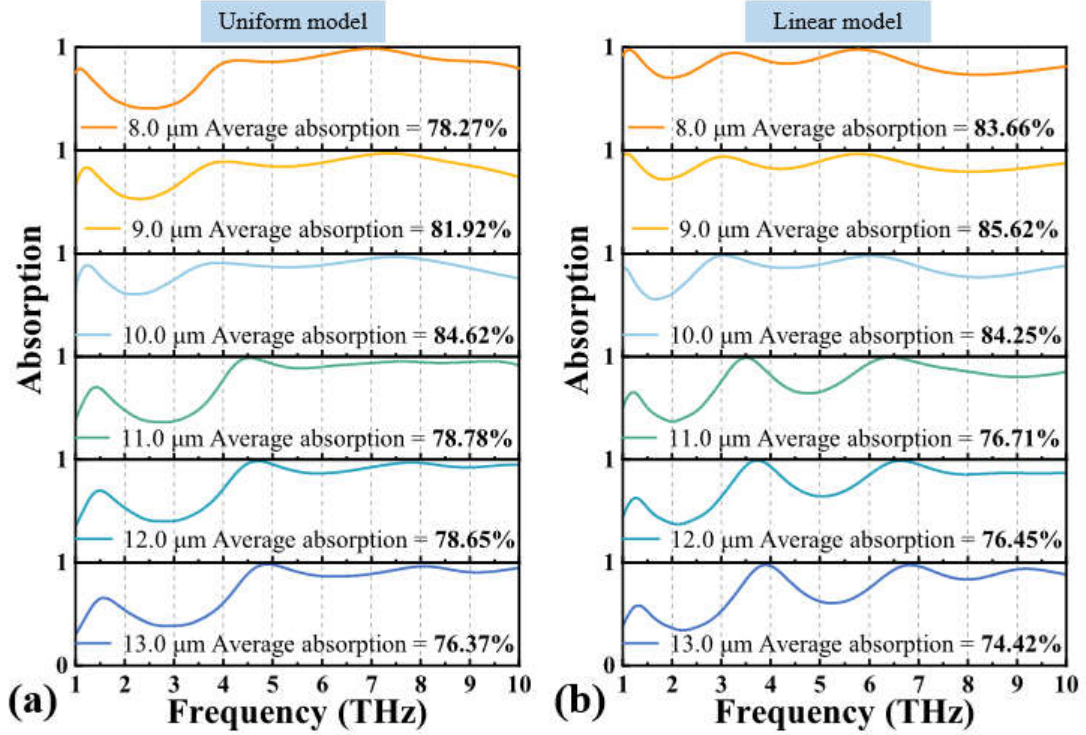**FIG. S8.** Absorption spectra of the two models at different h. (a) Uniform model. (b) Linear model.
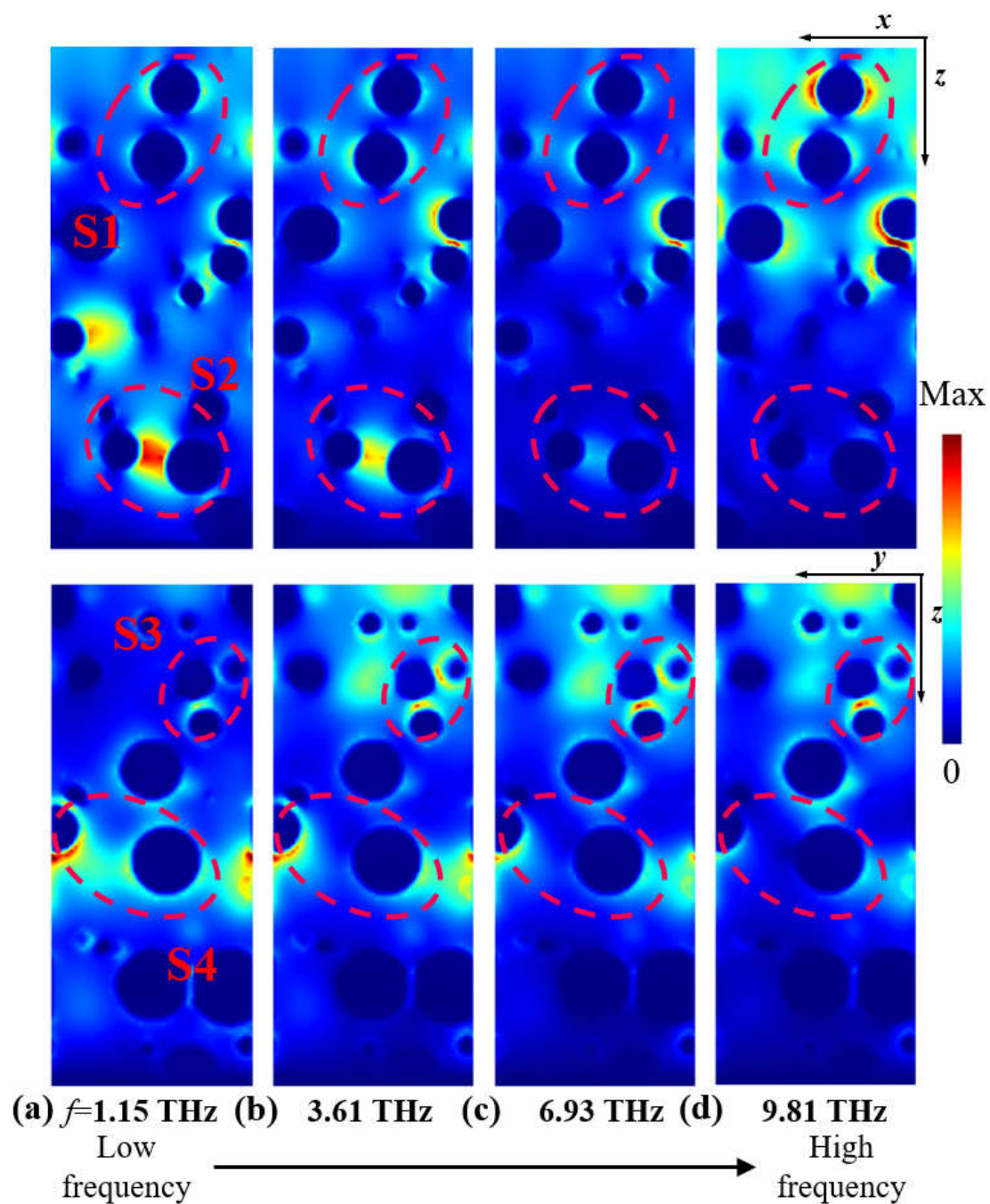

FIG. S9. Absorption spectra of the two models at different P. (a) Uniform model. (b) Linear model.

SM7: Electric field distributions in the x-z and y-z planes

FIG. S10. Distributions of electric fields in the frequency and spatial regions of the *x-z* plane and *y-z* plane in the uniform model are calculated. (a-d) 1.15 THz, 3.61 THz, 6.93 THz, and 9.81 THz. The red dashed circles indicate particular regions with significant evolutionary processes in the frequency domain.
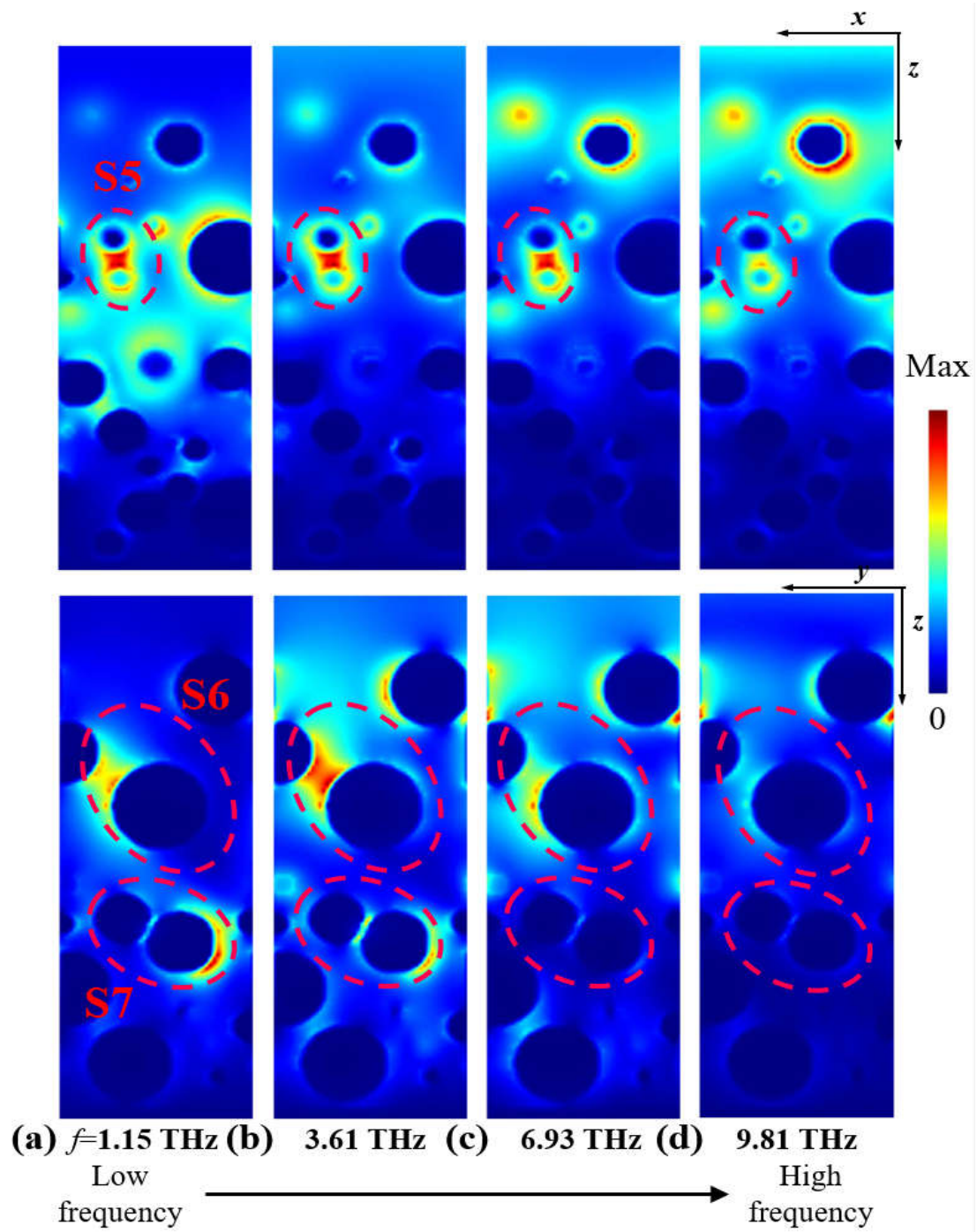
FIG. S11. Distributions of electric fields in the frequency and spatial regions of the *x-z* plane and *y-z* plane in the linear model are calculated. (a-d) 1.15 THz, 3.61 THz, 6.93 THz, and 9.81 THz.